Arch. Metall. Mater. **65** (2020), 1, 305-312

DOI: 10.24425/amm.2020.131731

LIN MA[1†], SHIYU NIU[1†], SHUDE JI[1*], PENG GONG[1]

COMPARATIVE STUDY OF 2060-T8 Al-Li ALLOY FRICTION STIR WELDED JOINTS BETWEEN NATURAL COOLING AND WATER COOLING

2060-T8 Al-Li alloy was friction stir butt welded under natural and water cooling conditions. Microstructures and mechanical properties of the welding joints were mainly compared and discussed. By spraying water on the top surface of stir zone, the grain size was reduced, attributing to the improvement of microhardness. The maximum tensile strength under the water cooling reached 461.1 MPa. The joint fractured at the stir zone due to the thickness reduction and the joint softening. The fracture surface consisted of many dimples with various sizes, indicating the typical ductile fracture. The strategy to apply the low heat input at the welding stage and high cooling rate at the cooling stage during FSW is necessary to obtain a high-quality FSW joint.

Keywords: 2060-T8 Al-Li alloy; Friction stir welding; Water cooling; Microstructure; Mechanical properties

1. Introduction

Friction stir welding (FSW), a solid-state joining process invented by TWI (The welding institute) in 1991, has the advantage of high joint quality, low distortion, small residual stress and non-pollution [1,2]. FSW is preferentially selected to weld high-strength aluminum alloys or dissimilar materials due to low peak temperature and severe plastic deformation, and has been widely applied to aerospace, shipbuilding, rail transportation and other manufacturing fields [3-5].

Generally, FSW joint of similar or dissimilar materials is characterized by a higher strength compared to conventional welding joint [6,7]. A sound welding joint can be achieved, while a stir zone (SZ) with fine and equiaxed grains can be achieved via FSW. In order to obtain sufficient material flow in the SZ during FSW, high friction heat and plastic deformation heat are essential. However, excessive heat input leads to serious joint softening, thereby decreasing the joint strength [8-11]. In recent years, researchers have conducted many experimental studies using cooling mediums such as liquid nitrogen, liquid CO_2 and water to reduce the softening degree of joint and then improve the joint quality. Xu et al. [12] investigated the effect of the liquid CO_2 on the 70/30 brass FSW joint. They found that no obvious heat affected zone (HAZ) was observed and the SZ was featured by the fine grains. Liu et al. [13] improved the FSW joint strength of Ti-6Al-4V alloy by the liquid nitrogen, and the joint tensile strength of 1020 MPa was almost equal to that of base metal (BM). In fact, water is chosen as a common and easily-controlled cooling medium during FSW [8,14-18]. Liu et al. [8] studied underwater FSW of 2219-T6 aluminum alloy and pointed out that the softening region of the joint was remarkably narrowed, which was beneficial to improving the joint strength. Zhao et al. [14] indicated that the water cooling could effectively restrict the growth of the grains and precipitate phases, improving the mechanical properties of underwater FSW joint of 7055-T6 aluminum alloy. Cai et al. [16] studied in-process water cooling FSW with two water spraying heads of 2060-T8 aluminum alloy and achieved the maximum tensile strength of 435 MPa. According to the published literatures [8,14-18], the water cooling FSW processes include underwater FSW and spraying water on the top surface of FSW joint. During FSW, the materials of the SZ top surface contact with rotating shoulder and then undergo a relatively high peak temperature due to the large fraction heat; the materials of the SZ bottom surface contacting with backing plate experience a lower peak temperature because of the rapid heat dissipation [19]. The temperature gradient along the thickness direction leads to the differences of material flow characteristic, grain size and precipitation behavior, resulting in a non-uniformity of joint quality along the thickness direction [13]. When the cooling medium

[1] SHENYANG AEROSPACE UNIVERSITY, SCHOOL OF AEROSPACE ENGINEERING, SHENYANG 110136, P. R. CHINA

* Corresponding author: superjsd@163.com

† Shiyu Niu and Lin Ma contributed equally to this work

acts on the top surface of the joint, the cooling rate at the SZ top is greatly increased, which is conductive to reducing the temperature gradient along the thickness direction. Therefore, spraying water, as an intense cooling source that is applied to the top surface of the SZ, is better than the underwater process only from the viewpoint of reducing temperature gradient along the thickness direction.

2060 Al-Li alloy is one of the third-generation Al-Li alloys [16,20]. Similar to other high strength Al alloys [21,22], 2060 alloy cannot be joined by fusion welding because of the volatilization of Li element with a low melting point. Nowadays, there are a few researches on FSW of 2060 Al-Li alloy. Some researchers have studied effects of water cooling and rotating velocity on the joint formation and mechanical properties [16,23]. The effect of liquid nitrogen cooling on residual welding stress has also been studied [24]. However, there is no report about the systematic comparison of 2060 Al-Li alloy FSW joints between natural cooling and water cooling conditions. In this study, FSW joints of 2060-T8 Al-Li alloy under the natural cooling and water cooling conditions were investigated. The microstructural evolution, microhardness and tensile properties of the joints were compared in detail.

2. Experimental procedure

2060-T8 Al-Li alloy plates with a thickness of 2 mm were used as the BM, whose dimensions were 200 mm×100 mm. The chemical compositions of the BM mainly include Cu 3.95, Li 0.75, Mg 0.85, Ag 0.25, Zr 0.11, Mn 0.3, Zn 0.4 and Al balance (all in mass %). 2060-T8 alloy plates were friction stir butt welded by the FSW machine (FSW-3LM-4012), and this machine was produced by Beijing FSW Technology Co., Ltd. The welding direction was perpendicular to the rolling direction of the welded plates. Two cooling conditions were adopted. One was natural cooling, and the other was water cooling. Fig. 1a displays schematic of the water cooling FSW. The rotating tool and the welding process parameters under the natural cooling and the water cooling were all the same. The rotating tool was made of H13 steel, and consisted of a concentric-circle-flute shoulder and a screwed pin (Fig. 1b). A rotating velocity of 800 rpm and a welding speed of 200 mm/min were used on basis of the previous experiments [16,25]. A tilting angle of the rotating tool with respect to Z-axis was 2.5º and a plunge depth of the rotating shoulder was 0.15 mm. During the water cooling

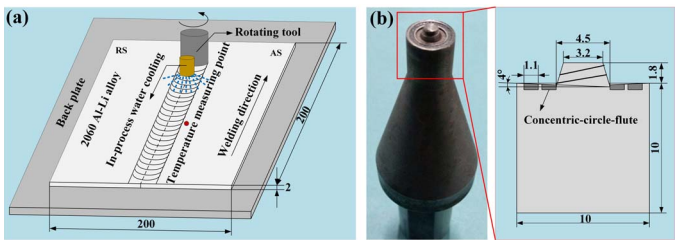

Fig. 1. (a) Schematic of water cooling FSW and (b) rotating tool (unit: mm)

FSW, the water with a spraying rate of 200 ml/min was sprayed on the top surface of the joint, while the distance between the cooling source and the rotating tool was 10 mm.

The metallographic and mechanical property specimens were cut perpendicular to the weld using a wire cutting equipment. After the specimens were burnished and polished, microstructure and microhardness were analyzed. The etching solution contained 3 ml HF, 6 ml HCl, 6 ml HNO_3 and 85 ml H_2O. The macrostructures in cross-section were observed by an optical microscope (GX71, OLYMPUS) at an etching time of 8s. The microstructures of the typical regions were observed by a scanning electron microscope (SEM, VEGATE-Scan) equipped with an energy-dispersive x-ray spectrometer (EDS). The measured positions of microhardness are shown in Fig. 2a. The microhardness tests were performed with a testing step of 0.5 mm, a load of 100 g and a dwell time of 15 s. Illustration of the tensile specimen with reference to GB/T 2651-2008 (ISO 4136:2001) is shown in Fig. 2b. Three tensile specimens for each welding process were prepared and the average values were used to evaluate. After performing the tensile test at the room temperature by a universal testing machine with a fixed tensile rate of 3 mm/min, the fracture morphologies were observed by a stereoscopic microscope (ZSA403) and the SEM.

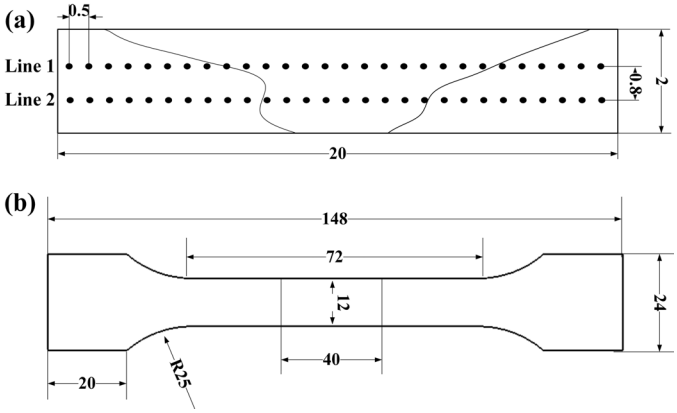

Fig. 2. Dimension drawings: (a) microhardness specimen and (b) tensile specimen (unit: mm)

3. Results

3.1. Macrostructure and microstructure

Fig. 3 presents the macrostructures in cross-sections of FSW joints under different cooling conditions. The defect-free joints are attained. Similar to other aluminum alloys [26,27], the FSW joints in this study can be divided into four zones: SZ, thermo-mechanically affected zone (TMAZ), HAZ and BM. The SZs in Fig. 3 present a “bowl” shape at the advancing side (AS). However, the SZ at the retreating side (RS) shows many differences because the materials in the TMAZ extend into the SZ. This phenomenon was also reported by Liu et al. [23]. Compared with the natural cooling, the distance of the materials

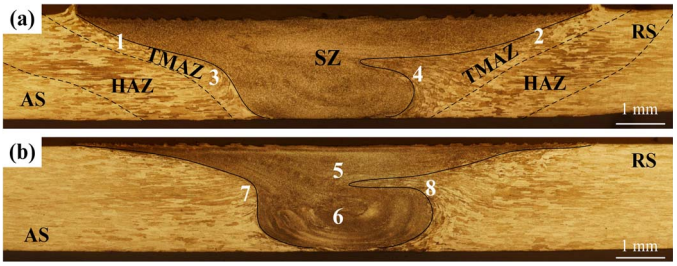

Fig. 3. Macrostructures in cross-sections of joints: (a) natural cooling and (b) water cooling

in the TMAZ extending into the SZ increases under the water cooling. Moreover, the widths of the SZ top and center under the water cooling are respectively smaller and larger than those under the natural cooling.

Fig. 4 displays the microstructures of the joint under the natural cooling. The microstructure of the BM in Fig. 4a presents an elongated pancake-like structure along the rolling direction. The HAZ only undergoing thermal cycle is featured by the coarsened grains. During FSW, dynamic recrystallization (DRX) always occurs in the SZ due to the combination effect of severe thermo-mechanical behavior [28,29]. Certainly, DRX also occurs in the present study, and the microstructure in the SZ is characterized by the fine and equiaxed grains (Fig. 4c and d). The average grain size in the SZ top (Fig. 4c) is 7.74 μm, which is 3.49 μm bigger than that in the SZ center (Fig. 4d).

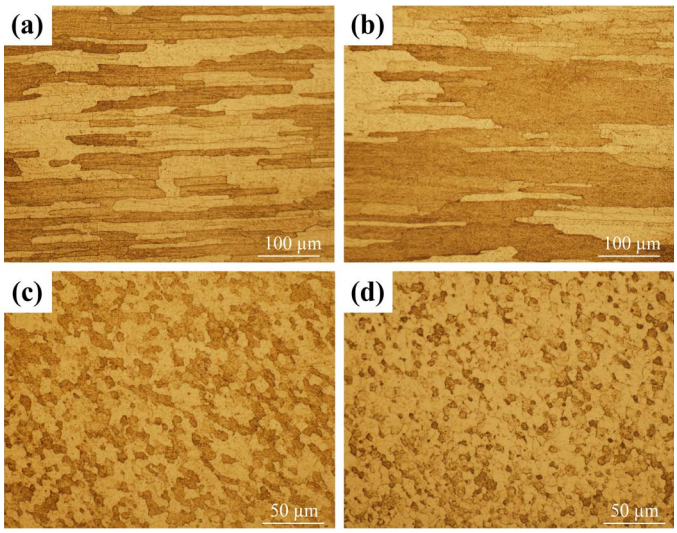

Fig. 4. Microstructures of the joint by natural cooling: (a) BM, (b) HAZ, (c) SZ top and (d) SZ center

Fig. 5 displays the microstructures of the typical regions in the TMAZ under the natural cooling condition. The interface between the TMAZ and the SZ at the AS is clearer than that at the RS. The grains in the TMAZ of the joint top are mainly distributed parallel to joint surface (Fig. 5a and b). The microstructures in the TMAZ of the joint center present the elongated and bended grains (Fig. 5c and d). The difference of grain morphology between the SZ top and bottom is mainly related to the material flow behavior in TMAZ (Fig. 5e). In addition, the materials at the RS in Fig. 5d undergo bigger transfer displacement than those at the AS in Fig. 5c, which was also reported by Ji et al. [30].

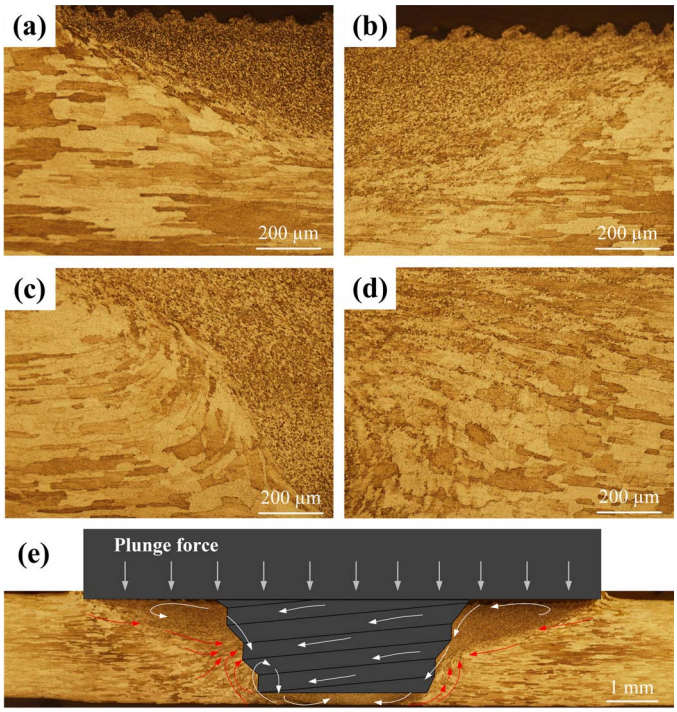

Fig. 5. Microstructures in the TMAZ by natural cooling: (a) region 1, (b) region 2, (c) region 3 and (d) region 4 marked in Fig. 3a; (e) schematic illustration of material flow model

Fig. 6 presents the microstructures of the typical regions in the SZ and the TMAZ under the water cooling. It is noteworthy that the grain sizes at the SZ top (Fig. 6a) and the SZ center (Fig. 6b) are respectively 2.97 μm and 2.27 μm, which are smaller than those of the natural cooling joint (Fig. 4c and d). Compare with the natural cooling, the grain size between the SZ top and the SZ center under the water cooling varies slightly,

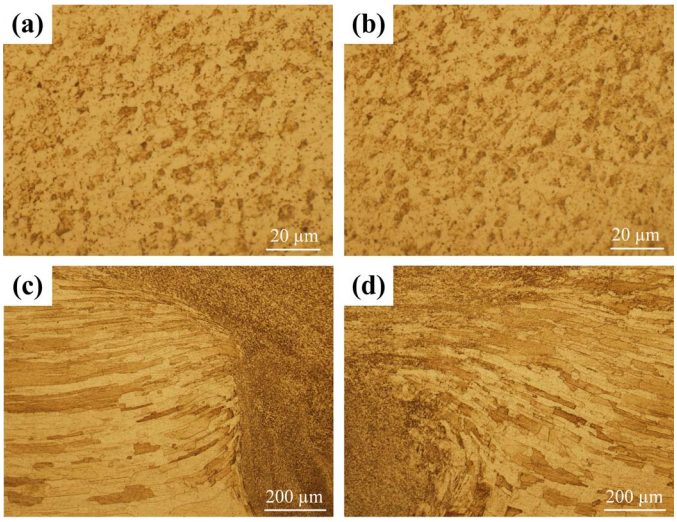

Fig. 6. Microstructures of the joint by water cooling: (a) region 5, (b) region 6, (c) region 7 and (d) region 8 marked in Fig. 3b

only 0.7 μm. The grains in the TMAZ center under the water cooling in Fig. 6c and d present the longer and thinner shape compared to those under the natural cooling in Fig. 5c and d. In fact, the differences of the microstructures between the two different cooling conditions influence the mechanical properties, which will be discussed in the following section.

Fig. 7 exhibits the distribution of strengthening phase particle in the joints. The white particles with a large size are considered possibly to be the S' (Al_2CuMg) phase according to the point scanning and line scanning results in Fig. 7c and f. The S' phase with various sizes randomly distribute in the BM, and phase size in the HAZ become larger than that in the BM (Fig. 7a and b). The S' phase cannot be observed in the SZ under two cooling conditions, as shown in Fig. 7d and e.

3.2. Microhardness

Fig. 8 presents the microhardness distributions of the FSW joints under different cooling conditions. Similar to other aluminum alloys [31], the microhardness distribution present a "W" shape. The average microhardness value of the BM is 162 HV. The SZ with the fine DRX grain possesses higher microhardness compared to the TMAZ. The average microhardness value of the SZ under the water cooling is higher than that under the natural cooling. The minimum microhardness locates at the boundary between the HAZ and the TMAZ at the RS, and its value under the water cooling is 125.3 HV which is 3.2 HV higher than that under the natural cooling. Especially, for the points in Fig. 8a with about 1~3 mm from the SZ center at the RS, the measured

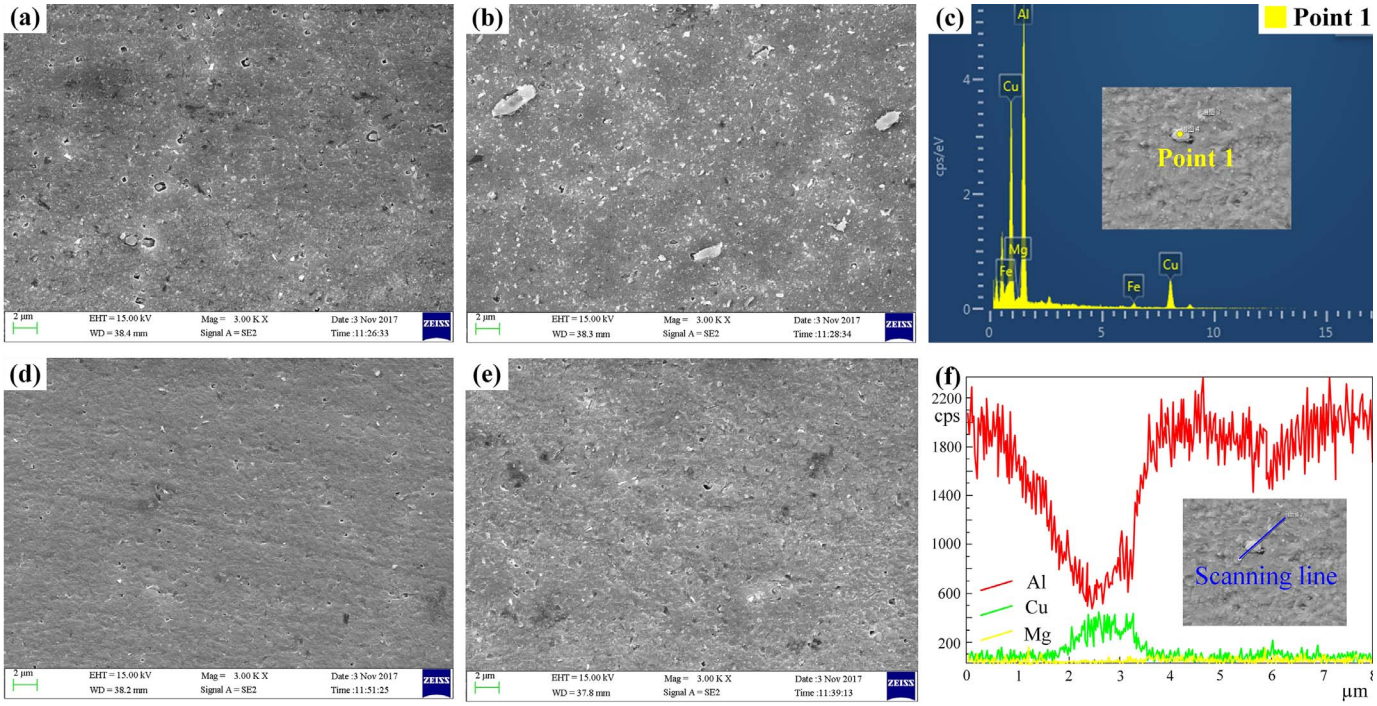

Fig. 7. Strengthening phase particle in the joints: (a) BM; (b) HAZ under natural cooling; (d) and (e) SZs under natural cooling and water cooling; (c) and (f) EDS analyses of this particle

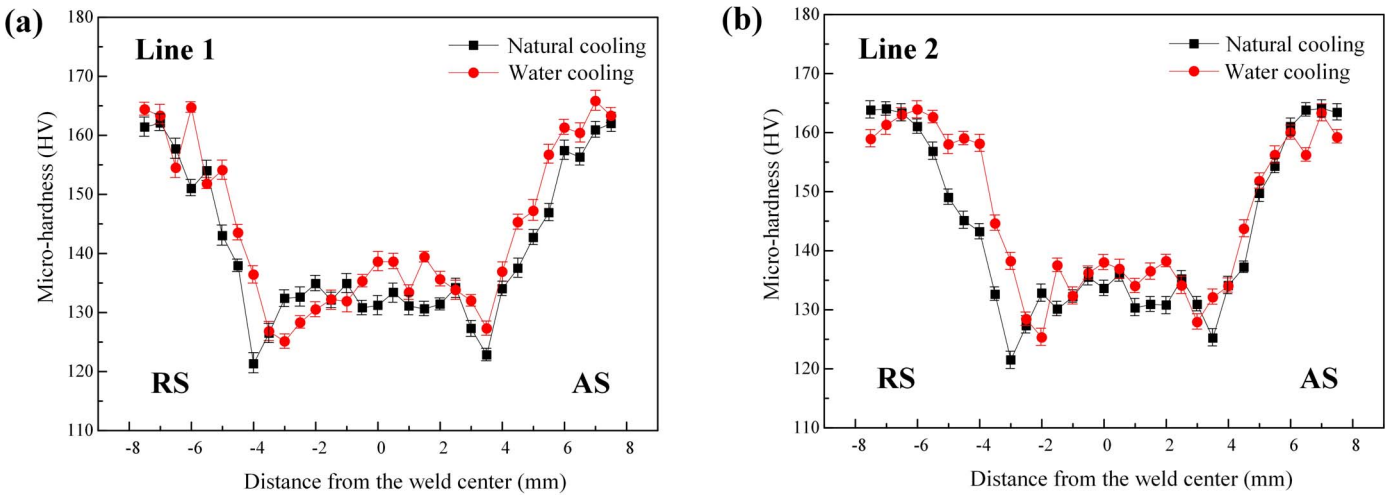

Fig. 8. Microhardness profiles on cross-sections of joints using two cooling processes: (a) line 1 and (b) line 2

hardness values under the water cooling are all lower than those under the natural cooling. As a whole, the joint under the water cooling has a narrower softening region and a lower softening degree.

3.3. Tensile properties

Fig. 9 displays the tensile properties of the FSW joints. Due to the joint softening phenomenon, the FSW joints possess lower tensile properties than the BM. Under the natural cooling, the maximum tensile strength and elongation of the joint are respectively 421.3 MPa and 3.3%. The maximum tensile strength and elongation of the FSW joint under the water cooling respectively reach 461.4 MPa and 6.8%, which are far higher than those of the joint under the natural cooling. Fig. 10 presents the fracture morphologies of the joints. The fracture positions of the joints under two cooling conditions both locate at the SZ, as shown in Fig. 10a and b. The fracture surfaces of the joints are composed of dimples with various sizes and depths, while a little bright phase particles can be observed in some dimples at the SZ center of the water cooling joint (Fig. 10c and d). These fracture morphology characteristics indicate that the two different FSW joints exhibit the good ductility.

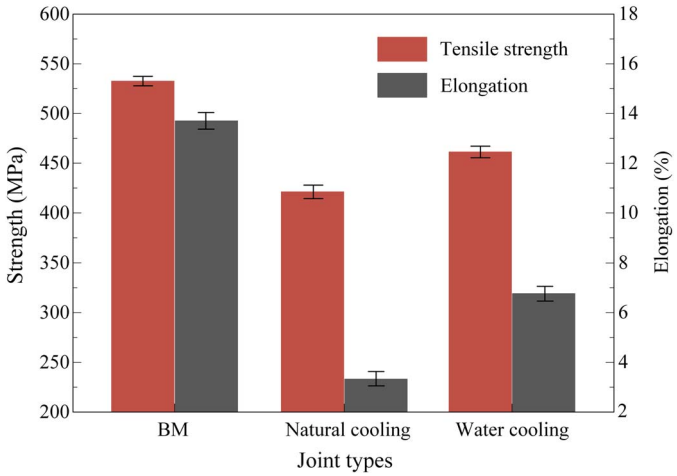

Fig. 9. Tensile testing results

4. Discussion

The differences of joint formation and microstructure between the different joints are affected by temperature evolution during welding process. In this study, the temperature was measured using the K-type thermocouples, and the measured point was 6 mm away from the welding centerline (Fig. 1a). Fig. 11 displays the temperature cycles under different cooling conditions. The peak temperature under the water cooling is 295°C, which is 42°C lower than that under the natural cooling. Compared to the natural cooling, the temperature cycle under the water cooling presents a sharp drop at the cooling stage, which means that the water cooling reduces the growth time

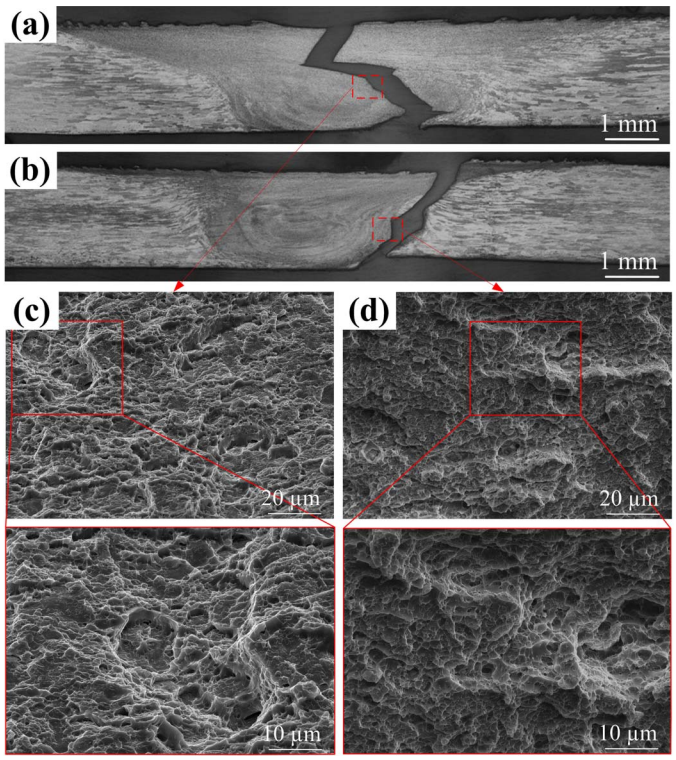

Fig. 10. Fracture morphologies of joints: (a) and (c) by natural cooling; (b) and (d) by water cooling

of microstructures. These differences about the temperature between the two cooling conditions lead to the differences of the joint formation and the microstructure.

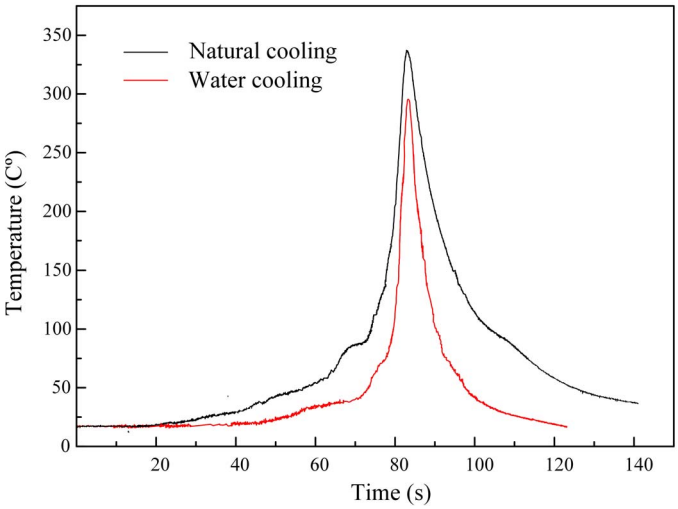

Fig. 11. Temperature measurement results under different processes

During the water cooling process, the water spraying on the top surface of the SZ results in a low peak temperature (Fig. 11), which heightens the flow stress of the materials. Therefore, the width of the top region of the SZ under the water cooling is smaller than that under the natural cooling. Compared with the natural cooling (Fig. 3a), the materials with a relatively large flow stress in the SZ top greatly restrain the materials in the SZ center to flow upwards under the water cooling, leading to

a higher flow velocity of the materials in the SZ center and then enlarging the SZ center (Fig. 3b). For the conventional rotating tool in Fig. 1b, the frictional heat generated by the rotating shoulder is much larger than that by the rotating pin, which causes that the materials in the SZ top undergo a higher temperature than those in the SZ center [32]. This is the reason why the grain size in the SZ top is larger than that in the SZ center (Figs. 4 and 6). It is known that changing cooling condition cannot change the DRX phenomenon in the SZ. Ji et al. [24] reported that the rapid cooling behind the rotating tool slightly reduced the peak temperature in the SZ, and increased the cooling rate at the cooling stage, which agrees with the experimental results in Fig. 11. For the water cooling process, the lower peak temperature and the higher cooling rate are beneficial to shortening the growth time of the grains compared to the natural cooling. This is the reason why the grain size of the SZ under the water cooling is distinctly smaller than that under the natural cooling (Figs. 4 and 6).

When a right-screwed rotating pin rotates anticlockwise, the materials contacting with the rotating pin flow downwards, and then accumulate near the pin tip during FSW [33]. The accumulated materials push and transfer the materials in the TMAZ upwards. The rotating shoulder always plunges into the welded plates to attain sufficient heat input, which loads a downward force on the TMAZ and then transfers the materials in the TMAZ downwards. Therefore, the grain morphology in the TMAZ top is different from that in the TMAZ center (Fig. 5). As mentioned above, the materials in the SZ center under the water cooling flow more violently than those under the natural cooling, resulting in the longer and thinner grains in the TMAZ (Fig. 6c and d). From the above-mentioned results, the inconsistency of the grain sizes in each zone is unavoidable for the FSW joint due to the thermal-mechanical behaviors. Stress concentration occurs at the interface with the large difference of grain size when the joint is subjected to an external load, which is not conducive to the service performance of joint in practical engineering applications [34]. In fact, the inconsistency of the grain size also exists in the FSW joints of other high-strength aluminum alloys, which has been accepted in practical engineering structures.

Besides the difference in grain morphology, the evolution of strengthening phase is one of the key factors affecting the joint quality. 2060-T8 Al-Li alloy belongs to one of the precipitation strengthening alloys. In fact, the type and amount of precipitates particles are relative to the composition and the heat treated state of Al-Li alloy. The precipitates of Al-Li alloy mainly contain T_1 (Al_2CuLi), θ' (Al_2Cu), δ' (Al_3Li), β' (Al_3Zr), S' (Al_2CuMg) phases [16]. During FSW, the high frictional heat easily results in the dissolution and re-precipitation of the strengthening phases. Because the materials in the HAZ undergo the thermal cycle which comes from the conduction of heat input in the SZ, the S' phase in the HAZ are characterized by the coarsening morphology, as shown in Fig. 7b. Fonda et al. [35] revealed the precipitation processes during FSW and stated that the original precipitates complete dissolved in the TMAZ which experienced the higher temperature, and then new precipitates such as δ'/β' formed from the supersaturated substrate in proportion to the amount of original particle dissolution. Moreover, the S′ phase in the SZ are broken and dissolve at the welding stage due to the stirring action of rotating tool and the high heat input (Fig. 7d and e). This result is consistent with the studies by Cai et al. and Liu et al. [16,23]. According to the research results of Liu et al. [23], the re-precipitates in the SZ were mainly T_1, δ' and β' phases (Fig. 12), and the volume fraction of those phases reduced with the increase of the rotating velocity. In fact, the peak temperature in the SZ increases with the increase of the rotating velocity under a constant welding speed. The higher heat input leads to the smaller volume fraction of phases in the SZ. Similarly, the heat input in the SZ under water cooling in this study is smaller than that under natural cooling (Fig. 11), so the volume fraction of the re-precipitates in the SZ under the water cooling can be considered to be larger. The precipitates pose a hindrance to the movement of dislocations [36,37]. Therefore, it can be concluded that the water cooling process is contributed to increasing the joint strength by improving the precipitates evolution from the viewpoint of controlling heat input.

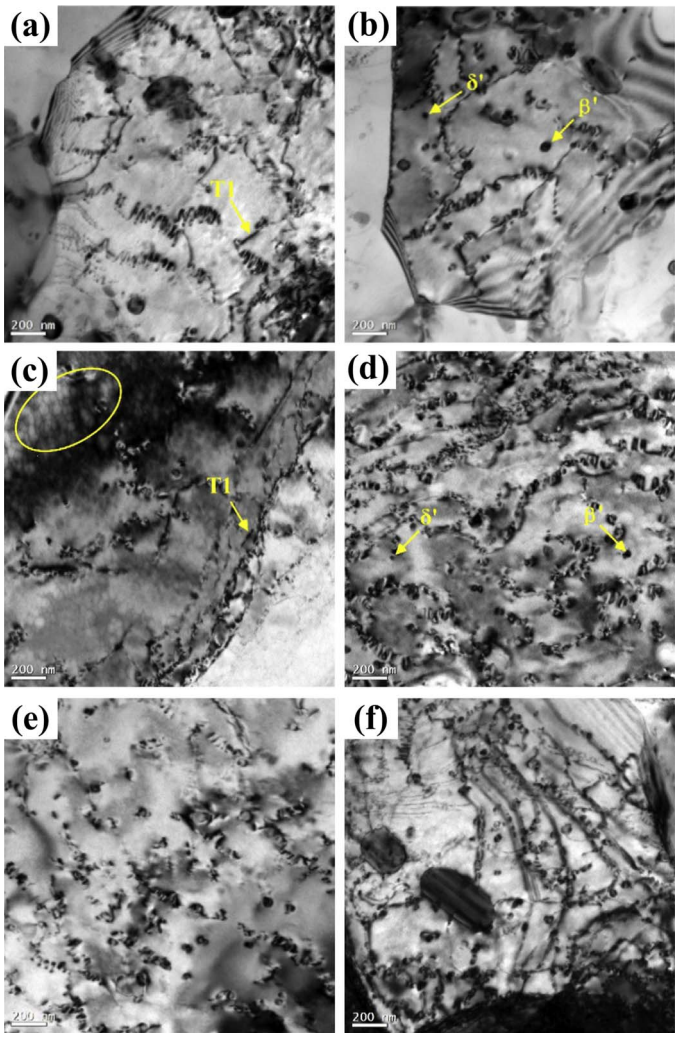

Fig. 12. The re-precipitates in the SZs of the joints under different rotating velocities in the research by Liu et al. [23]: (a) and (b) 600 rpm; (c) and (d) 800 rpm and (e) and (f) 1000 rpm

The differences in the microstructures under different cooling conditions influence the mechanical properties of the FSW joint. Besides the precipitates evolution, the softening degree of the joint is also related to the grain size, which can be explained by the Hall-Petch relation [13]. For the water cooling process, the SZ is characterized by the finer grains compared to the natural cooling (Figs. 4 and 6). Therefore, a higher average microhardness occurs in the SZ by the water cooling. Although the water is only sprayed on the top surface of the SZ, the materials in the HAZ and the TMAZ both undergo lower peak temperature and higher cooling rate (Fig. 11). The grain refinement and the lower coarsening degree of phase particle in the HAZ narrow the softening region and reduce softening degree of the joint under the water cooling undergoing the relatively short thermal cycle (Fig. 8). The tilting angle and the plunge depth of the rotating tool result in the thickness reduction of welding joint. The thickness reduction is a one of the factors influencing tensile strength of FSW joint [38,39]. The SZ has a smaller area of load bearing compared to the TMAZ and the HAZ. Therefore, although the microhardness in the SZ is slightly higher than that in the TMAZ or the HAZ, the SZ is the weakest region during tensile test.

From the above-mentioned results, it is known that the water cooling is beneficial to reducing the width of softening zone and the softening degree, which improves the tensile properties. Therefore, the joint under the water cooling achieves higher tensile properties than that under the natural cooling. Compared with the natural cooling, the dimples on the fracture surface of the joint under the water cooling have the larger depth, indicating the better ductility (Fig. 10). Generally speaking, a larger elongation of the joint always reflects a better ductility. From Fig. 9, the elongation of the joint under the water cooling is larger than that under the natural cooling, which is in agreement with the difference of fracture surface morphologies (Fig. 10c and d). In summary, the both joints under the two cooling conditions present the typical ductile fracture, and the welding joint has a better ductility when the water cooling is used. By contrasting the published literatures by Cai et al. [16] and Liu et al. [23], the FSW joint of 2060 Al-Li alloy under the water cooling in this study has a higher tensile strength, as listed in Table 1. This is because that the heat input used in this study is lower and the spraying water increases the cooling rate. Therefore, it can be concluded that the combined effects of the reasonable low heat input at the welding stage and high cooling rate at the cooling stage during FSW are beneficial to obtaining a high-quality joint.

TABLE 1

A summary of tensile properties of FSW joints of 2060-T8 Al-Li alloys

Reference	Material	Rotating velocity (rpm)	Welding speed (mm/min)	Tensile strength (MPa)	Elongation (%)
Liu et al. [23]	2060-T8	800	300	440	2.8
Cai et al. [16]	2060-T8	2400	100	435	7.8
This study	2060-T8	800	200	461.4	6.8

5. Conclusions

2060-T8 Al-Li alloy was friction stir butt welded under the natural and water cooling conditions. Joint formation, microstructure, microhardness and tensile properties were mainly investigated. The following conclusions can be extracted.

(1) The materials in the thermo-mechanically affected zone at the retreating side extended into the stir zone. This extending distance was increased under the water cooling. Compared to the natural cooling, the widths of the top and the center of the stir zone were respectively reduced and increased.

(2) Under the water cooling, the grain size in the stir zone was fined, while the width of the softening region and the softening degree of the joint were reduced.

(3) The joint tensile strength of 461.4 MPa and the elongation of 6.8% under the water cooling were far higher than those of the joint under the natural cooling. The fracture surface morphologies in the stir zone of the joints were featured by the dimples, presenting the typical ductile fracture.

Acknowledgement

This work is supported by the National Natural Science Foundation of China (No. 51705339), the China Postdoctoral Science Foundation (No.2016M590821) and the Guangdong Provincial Key Laboratory of Advanced Welding Technology for Ships (No.2017B030302010).

REFERENCES

[1] L. Wan, Y.X. Huang, Z.L. Lv, S.X. Lv, J.C. Feng, Mater. Des. **55**, 197-203 (2014).

[2] V.C. Sinha, S. Kundu, S. Chatterjee, Arch. Metall. Mater. **62** (3), 1819-1825 (2017).

[3] M. Balamagendiracarman, S. Kundu, S. Chatterjee, Arch. Metall. Mater. **62** (3), 1813-1817 (2017).

[4] Y.X. Huang, X.C. Meng, Y.M. Xie, L. Wan, Z.L. Lv, J. Cao, J.C. Feng, Compos. Part A-Appl. S. **105**, 235-257 (2018).

[5] B. Rams, A. Pietras, K. Mroczka, Arch. Metall. Mater. **59** (1), 385-392 (2014).

[6] Y. Lin, Z.Q. Zheng, Mater. Charact. **123**, 307-314 (2017).

[7] S.Y. Niu, S.D. Ji, D.J. Yan, X.C. Meng, X.H. Xiong, J. Mater. Process. Technol. 263, 82-90 (2019).

[8] H.J. Liu, H.J. Zhang, L. Yu, Mater. Des. **32**, 1548-1553 (2011).

[9] P.L. Niu, W.Y. Li, X.W. Yang, A. Vairis, Sci. Technol. Weld. Joi. **23**, 58-62 (2018).

[10] A. Simar, Y. Bréchet, B.D. Meester, A. Denquin, T. Pardoen, Mater. Sci. Eng. A **486**, 85-95 (2008).

[11] M.J. Starink, A. Deschamps, S.C. Wang, Scripta. Mater. **58**, 377-382 (2008).

[12] N. Xu, R. Ueji, H. Fujii, Mater. Sci. Eng. A **610** (2), 132-138 (2014).

[13] Z.L. Liu, Y. Wang, S.D. Ji, Z. Li, Mater. Sci. Technol. **34**, 209-219 (2018).

[14] Y .Zhao, Q. Wang, H. Chen, K. Yan, Mater. Des. **56**, 725-730 (2014).
[15] Z. Zhang, B.L. Xiao, Z.Y. Ma, Mater. Sci. Eng. A **614** (37), 6-15 (2014).
[16] B. Cai, Z.Q. Zheng, D.Q .He, S.C. Li, H.P. Li, J. Alloy Compd. **649**, 19-27 (2015).
[17] K. Krasnowski, Arch. Metall. Mater. **59** (1), 157-162 (2014).
[18] Z. Zhang, B.L. Xiao, Z.Y. Ma, Mater. Charact. **106**, 255-265 (2015).
[19] Y.M. Yue, Q. Wen, S.D. Ji, L. Ma, Z. Lv, High Temp. Mat Pr-isr. **36** (7), 733-739 (2016).
[20] Y. Mao, L. Ke, F. Liu, C. Huang, Y. Chen, Q. Liu, Int. J. Adv. Manuf. Tech. **81**, 1419-1431 (2015).
[21] T.L. Jolu, T.F. Morgeneyer, A. Denquin, A.F. Gourgues-Lorenzon, Int. J. Fatigue **70**, 463-472 (2015).
[22] F.F. Wang, W.Y. Li, J. Shen, S.Y. Hu, J.F.D. Santos, Mater. Des. **86**, 933-940 (2015).
[23] H.J. Liu, Y.Y. Hu, C. Dou, D.P. Sekulic, Mater. Charact. **123**, 9-19 (2017).
[24] S.D. Ji, Z.P. Yang, Q. Wen, Y.M. Yue, L. Zhang, High Temp. Mat. Pr-isr. **37** (5), 397-403 (2017).
[25] W.F. Xu, Y.X. Luo, W. Zhang, M.W. Fu, Mater. Charact. **138**, 48-55 (2018).
[26] P.L. Niu, W.Y. Li, Z.H. Zhang, X. Yang, J. Mater. Sci. Technol. **9**, 987-990 (2017).
[27] Y.X. Huang, Z.L. Lv, L. Wan, J. Shen, J.F.D. Santos, Mater. Lett. **207**, 172-175 (2017).
[28] Y.C. Chen, H.J. Liu, J.C. Feng, Mater. Sci. Eng. A **420**, 21-25 (2006).
[29] Y.X. Huang, Y. Wang, L. Wan, H. Liu, J. Shen, J.F.D. Santos, Int. J. Adv. Manuf. Tech. **87**, 1115-1123 (2016).
[30] S.D. Ji, Y.Y. Jin, Y.M. Yue, S.S. Gao, Y.X. Huang, L. Wang, J. Mater. Sci. Technol. **29**, 955-960 (2013).
[31] H. Sidhar, N.Y. Martinez, R.S. Mishra, J. Silvanus, Mater. Des. **106**, 146-152 (2016).
[32] J.E. Gould, Z. Feng, J. Mater. Process. Manuf. Sci. **7**, 185-194 (1998).
[33] A. Sedaghati, H. Bouzary, P.I. Mech. Eng. L-J. Mater. (2017) DOI: 10.1177/1464420717726562 (in press).
[34] C. He, Y.J. Liu, J.F. Dong, Q.Y. Wang, D. Wagner, C. Bathias, Int. J. Fatigue **82**, 379-386 (2015).
[35] R.W. Fonda, J.F. Bingert, Metall. Mater. Trans. A **37** (12), 3593-3604 (2006).
[36] A.S. Zadeh, Mater. Sci. Eng. A **531**, 112-118 (2012).
[37] O. Myhr, Acta Mater. **49**, 65-75 (2001).
[38] A. Scialpi, M. De Giorgi, L.A.C. De Filippis, R. Nobile, F.M. Panella, Mater. Des. **29**, 928-936 (2008).
[39] Z.W. Ma, Y.Y. Jin, S.D. Ji, X.C. Meng, L. Ma, Q.H. Li, J. Mater. Sci. Technol. **35**, 94-99 (2019).